JATIS Journal of Astronomical Telescopes, Instruments, and Systems

RESEARCH PAPER

High-contrast demonstrations with the AstroPIC integrated photonic coronagraph

Rachel Morgan,[a,b,*] Eduardo Bendek,[a,b] Ruslan Belikov,[b] Kevin Fogarty,[b] Anne R. Kroo,[c] Carson Valdez,[c] Marek Vlk,[c] David A. B. Miller,[c] Olav Solgaard,[c] and Dan Sirbu[b,*]

[a]SETI Institute, Mountain View, California, United States
[b]NASA Ames Research Center, Moffett Field, California, United States
[c]Stanford University, Stanford, California, United States

ABSTRACT. Integrated photonics is a promising coronagraph technology option for exoplanet-imaging missions such as NASA's Habitable Worlds Observatory flagship. It is theoretically capable of achieving near-optimal coronagraphic performance because arrays of integrated interferometers can be controlled to implement any linear optical function with a device that is orders of magnitude smaller than the bulk optics equivalent. However, photonic coronagraphs require significant maturation to be ready for a space telescope mission. The AstroPIC project is advancing this technology by developing a proof of concept integrated photonic coronagraph based on silicon photonic integrated circuit (PIC) technology. In this paper, we summarize the design and implementation of the PIC coronagraph testbed at Ames, which is designed to be capable of measuring the target 100 dB extinction ratio required to observe an Earth-like planet around a Sun-like star. We present experimental results with the testbed that demonstrate a record-breaking on-chip extinction of a single input channel to $3.83 \pm 0.8 \times 10^{-10}$, or over 94 dB, using a nine-channel full triangular photonic mesh illuminated with 1550 nm wavelength light. We also demonstrate reimaging a circular pupil onto the input to the chip and implementing a mode sorting algorithm to achieve a contrast ratio of $8.7 \pm 1.1 \times 10^{-8}$, or over 70 dB, of the stellar source with a measured planet throughput of over 40% into the high-contrast channel.

© The Authors. Published by SPIE under a Creative Commons Attribution 4.0 International License. Distribution or reproduction of this work in whole or in part requires full attribution of the original publication, including its DOI. [DOI: 10.1117/1.JATIS.12.4.041042]

Keywords: coronagraphs; photonics; exoplanets

Paper 260043 received Jan. 28, 2026; revised Aug. 25, 2026; accepted Sep. 8, 2026; published Oct. 16, 2026.

1 Introduction

Integrated photonics has the potential to revolutionize optical instrumentation for astrophysics missions by fabricating many optical components on a common wafer substrate to produce instruments that are smaller, more robust to their environment, and more reconfigurable than bulk optics alternatives.[1] By leveraging recent advances in integrated photonics technology, a photonic integrated circuit (PIC) coronagraph instrument could be orders of magnitude smaller and significantly less mechanically complex than the bulk optics coronagraph instruments designed to date, which has potentially huge benefits for next-generation NASA astrophysics missions such as the Habitable Worlds Observatory.[2]

The AstroPIC coronagraph concept uses programmable photonics technology[3] to implement a universal linear optical device that includes an array of integrated Mach Zehnder

*Address all correspondence to Rachel Morgan, remorgan@alum.mit.edu; Dan Sirbu, dan.sirbu@nasa.gov

Interferometers (MZIs) that are cascaded in a "mesh" configuration with many programmable degrees of freedom that allow it to be configured to implement any linear optical operator.[4,5] This means that the device can theoretically be used to emulate any physically permissible optical system made up of linear components,[5] such as the lenses and masks used to implement traditional bulk-optics coronagraph designs. The large number of programmable degrees of freedom in a PIC coronagraph allows it to perform a more efficient mapping between the input and output electric field planes to reach closer to the theoretically optimal coronagraph operator at small inner working angles.[6–9]

Any traditional bulk-optics coronagraph or nulling interferometer architecture has a hard theoretical performance limit imposed by design constraints that cannot be overcome by technological advancements alone.[6] For example, coronagraph designs that use absorbing masks will never be able to recover any planet photons it irreversibly absorbs, and interferometers with a set number of subapertures cannot exceed the corresponding limit in angular resolution. Because a universal PIC coronagraph interferes the sampled input field rather than physically blocking any starlight, it faces no architectural constraints on its theoretical performance ceiling. The AstroPIC instrument is similar in operation to a nulling interferometer[10–13] with a large number of subapertures, but its programmability and universality distinguish it from existing nulling interferometer architectures. With sufficient technological maturation, a PIC coronagraph is theoretically capable of approaching the performance limit of an optimal coronagraph even at very small planet-star separation angles.[7,14]

The goal of a PIC coronagraph is to act as an extremely precise spatial mode filter that sorts starlight away from planet light with high extinction. Programmable integrated photonics is an attractive technology option to enable this type of filter device because it enables highly complex and actively controlled devices to be created with very small footprints.[3] Integrated photonic MZI mesh devices have been used in several recent demonstrations of high-precision sorting and manipulation of free-space optical fields.[15–17] Similar nonintegrated photonic mode sorting technologies have been proposed and demonstrated for astronomy applications, including spatial plane light converters for quantum-limited exoplanet detection[18] and photonic lanterns for nulling interferometry,[19,20] coherent imaging[21] and wavefront sensing.[22] Integrated photonics technology has also been applied to other types of astronomical instruments, including an extremely precise and compact glass photonic beam combiner for nulling interferometry[23] and miniaturized low-loss on-chip spectrometers.[24]

The AstroPIC coronagraph concept, shown in Fig. 1, demonstrates the utility of integrated photonics for exoplanet characterization by implementing a PIC-based coronagraph instrument.[25,14,26,27] Light is sampled from a telescope pupil plane using a microlens array that concentrates the light onto a 2D array of integrated grating couplers that couple the light into waveguides on the PIC. Once the light is coupled into on-chip waveguides, an array of tunable integrated MZIs can be controlled to interfere the input channels to implement any desired matrix operation on the input field to separate starlight from planet light. End-to-end simulations of the AstroPIC concept predict excellent high-contrast performance at small inner working angles while being much less sensitive to the telescope pupil shape compared to bulk-optics coronagraph designs.[27,28] The current nine-channel coronagraph prototype uses a 3×3 array of input grating couplers to sample light in a pupil plane, leading to a narrow outer working angle of $1.5\,\lambda/\mathrm{D}$ that can be increased in the future by increasing the number of input channels.[14,26,27] A companion paper in this edition describes the application of the AstroPIC concept to the Habitable Worlds Observatory mission in more detail.[14]

This paper describes the first high-contrast experiments demonstrated with the first-generation AstroPIC prototype instrument using the newly built PIC coronagraph testbed at NASA Ames Research Center. The design and implementation of the PIC testbed is described in Sec. 2. Section 3 summarizes two high-contrast experiments: first, a demonstration that reaches a record-breaking on-chip extinction ratio of $3.83 \pm 0.8 \times 10^{-10}$ for a single input channel illuminated with 1550 nm wavelength light, and second, a demonstration that achieves a raw contrast ratio of $8.70 \pm 1.1 \times 10^{-8}$ for a circular pupil coupled into the chip with monochromatic light at 1550 nm wavelength. These results also include data on the wavelength dependence of the high-contrast state and a demonstration of tilting the input source angle to measure the effective planet throughput into the high-contrast channel of over 40% at a star-planet separation of $1\,\lambda/\mathrm{D}$.

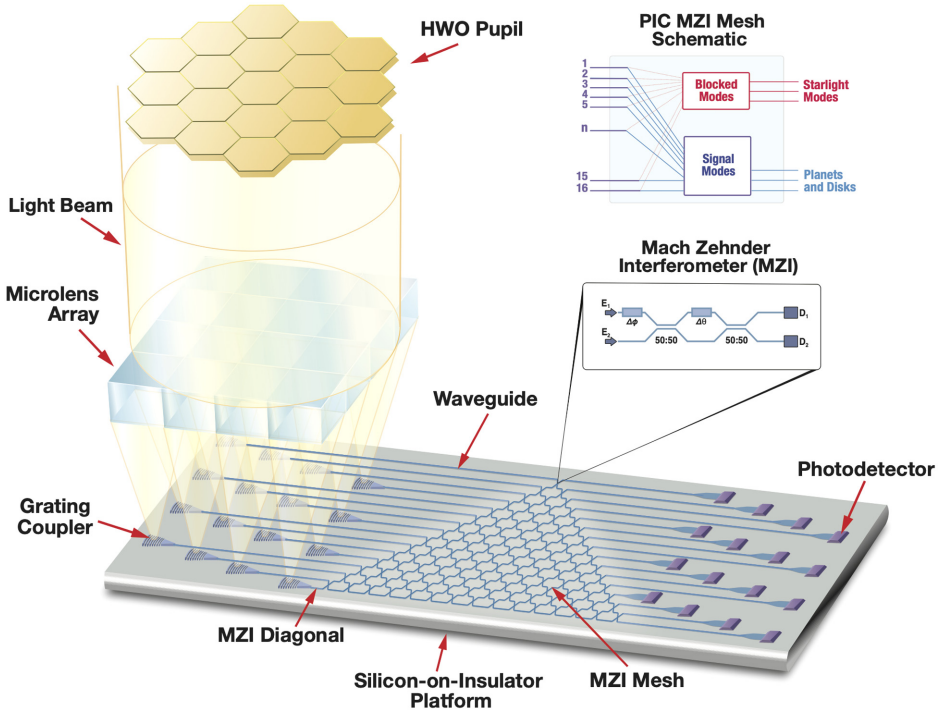


Fig. 1 Diagram of AstroPIC coronagraph concept: light is coupled from a telescope pupil plane into an integrated photonic chip using a microlens array and a 2D array of grating couplers. The PIC uses a mesh of MZIs to implement a near-optimal coronagraph operator to separate the planet light from the starlight.

Section 4 contains a discussion of the next steps for the AstroPIC project to scale the current prototype into a more useful astronomy instrument.

2 AstroPIC Testbed Design and Implementation

An integrated photonic coronagraph testbed has been developed at NASA Ames Research Center to characterize the performance of the AstroPIC instrument with realistic telescope pupil apertures and to identify the limiting factors that can be improved in future iterations of the instrument. The goal of the first-generation AstroPIC prototype instrument was to demonstrate the potential of the integrated photonic coronagraph concept by demonstrating an extinction ratio (ER) better than 90 dB (1×10^{-9}) for a single illuminated input channel and contrast better than 70 dB (1×10^{-7}) for a realistic HWO-like telescope pupil input.

To achieve these goals, the AstroPIC testbed was designed to be able to couple near-infrared light from a free space coupling module or single cleaved optical fibers onto the chip, control the 72 phase shifters contained in the nine-channel full triangular MZI mesh, and measure the readout from nine photodetectors simultaneously with >100 dB of dynamic range. The testbed also provides thermal control of the PIC and contains a top-view IR microscope and a side-view visible microscope for alignment and diagnostic visualization. More details on the testbed design and implementation can be found in Morgan et al. 2025.[25]

Figure 2 shows a diagram of the AstroPIC experimental setup and a photo of the testbed at NASA Ames Research Center. A near-infrared laser source (Optilab TWL-C-B, 1525 to 1565 nm wavelength range) is coupled to a single-mode optical fiber, and a half wave plate and quarter-wave plate are used to control the polarization of the light. A 99:1 fiber splitter is used to tap 1% of the light to be measured with a monitor photodiode in order to detect fluctuations in input laser power. The remaining 99% of the light is then coupled onto the chip with either a cleaved single-mode fiber, which is mounted on a custom fiber mount to maintain an input angle of 12 deg into a single grating coupler, or with a free-space coupling optics module that reimages a telescope pupil onto a microlens array that samples and concentrates the light onto the 2D 3×3 array of input grating couplers.[25]

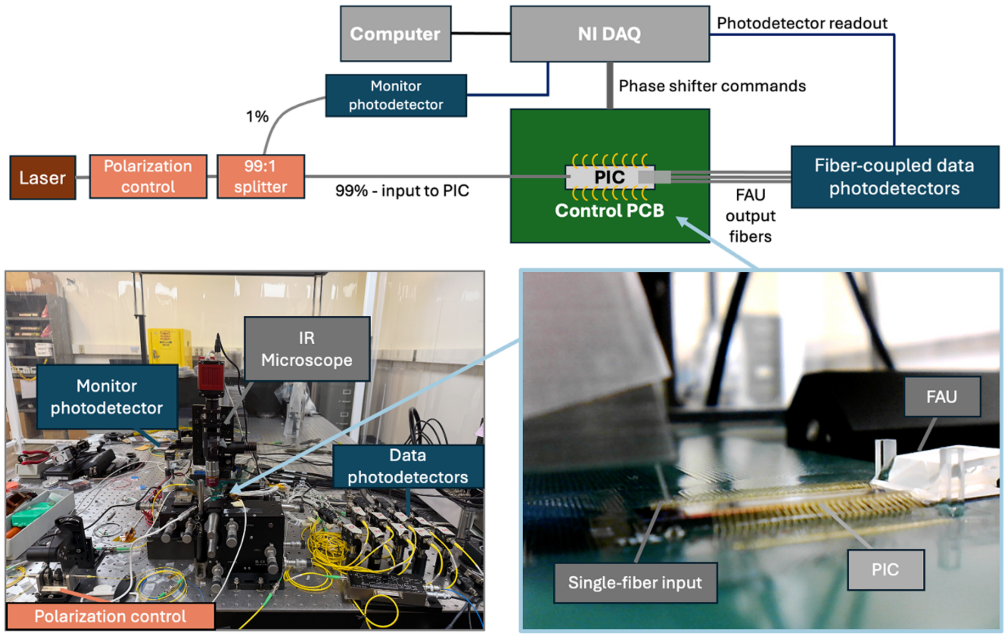


Fig. 2 (Top) Diagram of AstroPIC experimental setup. (Bottom left) Photo of the AstroPIC photonics testbed setup at NASA Ames. (Bottom right) Side-view photo of the PIC wirebonded to the control PCB with a single optical fiber aligned to the input and a fiber array unit (FAU) bonded to the output.

Light is coupled off the PIC with a 22-channel fiber array unit (FAU) that is bonded to the line of grating couplers at the output of the mesh. The output fibers are connected to nine individual photodetectors that are read out using an NI PXIe-6361 data-acquisition unit (DAQ). Most channels are designed for relatively high incident powers, corresponding to the stellar spatial modes that are orders of magnitude brighter than the signal planet modes. These "bright" channels are coupled to 8 Thorlabs DET01CFC InGaAs detectors with variable resistance terminators that are measured to have a sensitivity range of $\sim$7 nW $-$ 5 mW and can operate over a wavelength range of 800 to 1700 nm. One output channel is designated as the "high-contrast" channel and is coupled to a high sensitivity photodetector (Femto OE-200-IN2-FC, spectral range 900 to 1700 nm) with a variable gain amplifier that provides a measurement sensitivity of $\sim$100 fW $-$ 2 mW. An optical chopper can be placed in the path of the input signal between the half-wave plate and quarter-wave plate used for polarization control to modulate the signal so that the photodetector output can be fed to a SRS510 lock-in amplifier to increase the signal-to-noise ratio of the high-sensitivity output channel. This lock-in detection scheme enables the Femto photodetector to measure optical powers as low as $\sim$10 fW.

The PIC is epoxied and wirebonded to a host PCB that transmits the phase shifter control signals from an input connector onto the chip. The phase shifters are controlled with the NI PXIe-6361 DAQ using two PXIe-6739 cards installed to provide 128 control channels. Each channel has a voltage output of ± 10 V with 16-bit resolution. The PCB is mounted to a custom aluminum plate that contains a cutout underneath the PIC for a Peltier thermoelectric cooler (TEC) with 8.5 W max power draw (Same Sky model CP20251). The TEC is controlled with an Arroyo 5240 TEC controller that uses feedback from a thermistor on the host PCB near where the PIC is epoxied to provide thermal control to 0.01°C.

2.1 PIC Design and Fabrication

The first AstroPIC prototype design is a nine-channel full triangular photonic MZI mesh with the input grating couplers arranged in a 3×3 array to enable the input grating couplers to sample a telescope pupil plane. The first-generation AstroPIC chip design layout is shown in Fig. 3(b). The nine-channel full triangular mesh is shown with a dashed purple border and occupies a footprint of $\sim 13 \times 0.8$ mm. Schematics of the grating-to-grating and loopback test structures are also shown in Fig. 3(b). The grating-to-grating structure consists of a straight waveguide between

input and output grating couplers and is used to characterize the coupling loss. The loopback test structure connects two grating couplers on either end of the output line of the grating couplers with a single waveguide and is used for active alignment of the FAU.

The AstroPIC mesh is made with standard 220 nm tall × 500 nm wide silicon rectangular waveguides with silicon dioxide cladding. The chip uses thermal phase shifters for on-chip phase control, and air trenches are placed around the phase shifters to mitigate the effects of thermal cross-talk between nearby MZIs. The chip used in the experiments presented in this work was fabricated by the Applied Nanotools (ANT) foundry in Canada using their standard silicon-on-insulator processes. The ANT foundry uses electron beam lithography to pattern waveguide features, which can accommodate small feature sizes that enable the fabrication of high-efficiency inverse-designed grating couplers.[29,30]

2.2 Testbed Characterization

The Ames photonics testbed achieved first light with a PIC coronagraph in July 2025 using the chip shown in Fig. 3(a). The experiments presented here seek to characterize the performance of the components and systems on the chip and identify promising areas of improvement for future iterations of the chip and testbed designs.

The AstroPIC chip loss is dominated by coupling losses from the grating couplers that couple light from an optical fiber or the free-space input module into the waveguides. The coupling loss is measured to be 4.6 dB/coupler (35% efficiency per coupler) using cleaved single-mode fibers aligned to the input/output grating couplers of a straight waveguide test structure shown in Fig. 3(b). The insertion loss of the grating loss test structure is compared with the insertion loss of the two cleaved single mode fibers butt-coupled to each other, and the loss per coupler is calculated as $\left(\frac{L_{\text{grating2grating}} - L_{\text{fiber2fiber}}}{2}\right)$. The grating loss through the FAU is slightly higher because the polished fiber facets in the v-groove array are not able to reach as close to the grating couplers compared with a single cleaved fiber aligned above the chip. This coupling loss was measured to be 6.9 dB/coupler (20% efficiency) using the loopback test structure that connects two gratings at the outer edges of the output line of grating couplers [shown in Fig. 3(b)]. The other main source of loss is propagation loss due to material absorption or scattering in the silicon waveguides, which is measured to be 2.2 dB total loss (60% efficiency) for the 9 × 9 full triangular mesh, matching the expectation of ∼1 to 2 dB/cm propagation loss for SOI waveguides.

The full throughput of the chip is measured to be 3.6% (14 dB total loss) using a cleaved single-mode fiber at the input and a bonded FAU at the output. The fiber optics and polarization control components contribute an additional 1.6 dB of loss to the system, which means that the testbed has a measurable dynamic range of ∼100 dB (1×10^{-10}) with an input laser power of 40 mW and a minimum detectable power of ∼100 fW. With a circular pupil input, the measurable dynamic range of the testbed is reduced to 90 dB (1×10^{-9}) because additional losses are introduced by the pupil reimaging optics and coupling with the microlenses.

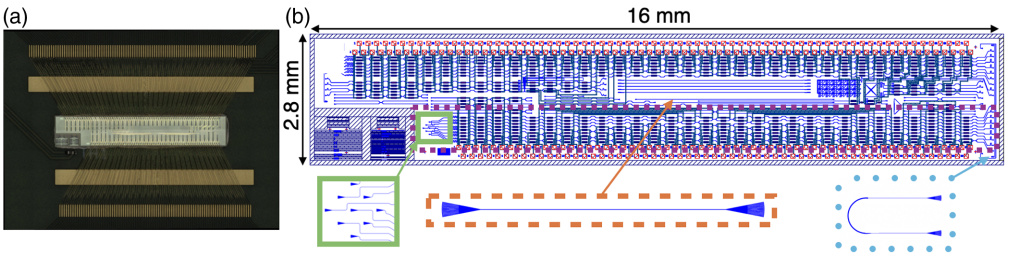


Fig. 3 (a) Photo of AstroPIC coronagraph prototype chip wirebonded to the host PCB. (b) Full PIC layout showing the nine-channel full triangular mesh with a dashed purple border and chip dimensions labeled. A zoomed-in view of the 3 × 3 input grating array and schematics of the grating-to-grating and loopback test structures used to characterize coupling losses are shown below the layout with arrows to their corresponding locations on the chip. Note: the loopback schematic is simplified, the actual device curves around the output line of grating couplers as shown on the right side of the layout.

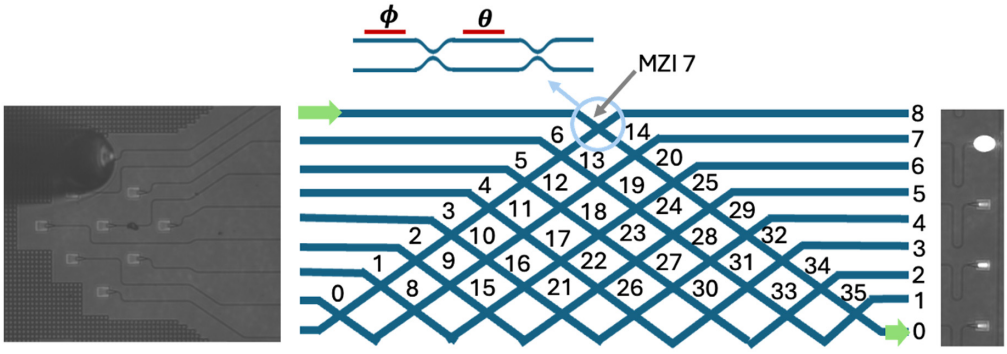


Fig. 4 Diagram of experimental setup for testbed characterization and single-channel minimization experiments showing (left) a photo of the input fiber aligned to the top input grating coupler, (center) a diagram of the nine-channel full triangular mesh with each MZI and output channel labeled with a number and a single MZI diagram inset to denote the ϕ and θ phase shifters, and (right) a photo of the output grating couplers for the bottom four channels illuminated with no voltage settings applied to the mesh.

Figure 4 shows a diagram of the nine-channel full triangular mesh of the first-generation AstroPIC chip prototype, with a schematic of a single MZI building block above. Before running any high-contrast experiments, the mesh was calibrated to find the bar (or pass-through) state for each MZI θ phase shifter. To do this, a single mode fiber was aligned to each input grating coupler in series starting from the top of the array (input 8 in Fig. 4). Then, each MZI in the corresponding diagonal (for input 8, this was MZI 7, 14, 20, 25, 29, 32, 34, and 35) was calibrated by sweeping the voltage applied to the θ phase shifter to find the setting that maximized the signal going to the top (bar) output of each MZI. These bar state voltage settings were saved to provide a precalibrated pass-through state that directly maps each input channel to the corresponding output directly across the chip, which is useful for testbed calibration and alignment. These settings were used to measure the coupling efficiency of each input/output channel individually, which varies by only $\sim$10% across the channels, likely due to a small tilt in the FAU alignment relative to the surface of the PIC.

The testbed was then used to characterize the MZI minimization routine, which follows the procedures described in Valdez et al. 2025,[31] where the optimal voltage for each phase shifter is found iteratively by sweeping the voltage across progressively smaller voltage ranges around the minimum state measured on the photodetector until the voltage sweep step size reaches the resolution limit of the DAQ (0.3 mV). Each photodetector measurement takes the average of 100 samples to reduce the influence of photodetector noise on the minimization routine.

Figure 5(a) shows the ER versus applied voltage, applying the minimization procedure to the θ phase shifter of MZI 7 and measuring output channels 0 and 8 (after having set MZIs 14 to 35 to a cross state to direct all light output from the bottom arm of MZI 7 to output channel 0). The ER is the ratio of each measurement to the maximum signal measured in the channel during the voltage sweep, which avoids complications due to potential differences in loss due to different grating coupler efficiencies between the two output channels. This measurement shows that the minimization routine can reach very high ERs by controlling just a single MZI, with a peak ER of 82.6 dB measured in the output diagonally across from the input (cross state) and 65.8 dB measured in the output directly across from the input (bar state). However, these minimum states are only achieved for a single voltage setting on the MZI, and small environmental changes, such as TEC temperature corrections, can lead to the signal drifting slightly, giving a repeatably stable ER of around 65 dB in cross and 45 dB in bar for each MZI.

Laboratory testing showed a strong dependence of achievable ER on the dwell time, which is the waiting time between applying a phase shifter voltage command and recording the corresponding photodetector measurement, as shown in Fig. 5(b). We believe this dependence results from longer dwells giving time for transient thermal effects to settle, while excessively long dwells leave time for environmental conditions to cause drift in the signal that degrades the performance. Based on these results, a dwell time of 0.1 s is used for most experiments, which means that the minimization routine takes about a minute to complete for each phase shifter.

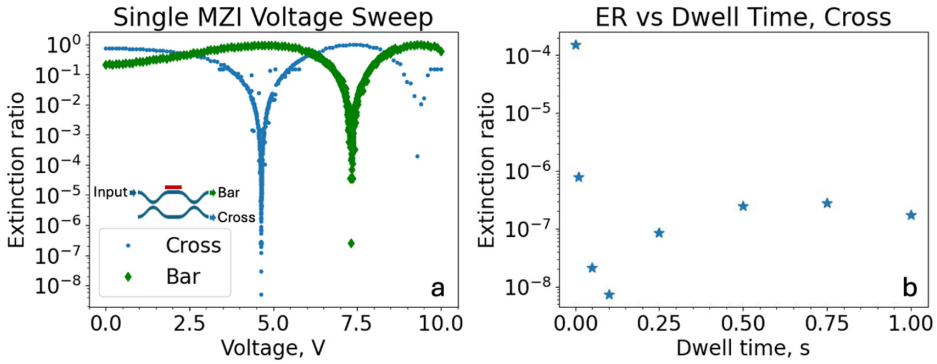


Fig. 5 (a) MZI transfer measurement using a chip fabricated by ANT showing a peak extinction ratio for a single controlled MZI of >80 dB measured in the output diagonally across from the input (cross state) and >60 dB in the output directly across from the input (bar state). The extinction ratio is defined relative to the maximum signal seen in each respective channel, and a small diagram explaining the bar versus cross state definition is included above the legend. (b) Minimization routine extinction ratio dependence on the dwell time between voltage commands and photodetector measurement. The data in (a) were taken with a dwell time of 0.1 s.

3 High-Contrast Experiment Results

3.1 Single Channel Minimization

The first type of coronagraph experiment performed with the Ames testbed used a cleaved single-mode fiber aligned to the grating coupler at the top of the input grating array and controlled the mesh to minimize the signal reaching the bottom output channel, as shown in Fig. 4. The total ER is defined as the signal measured in the output channel divided by the maximum possible signal that can be measured in that channel, which is calculated by multiplying the peak signal measured in the top output channel by a factor that accounts for a small difference in coupling loss between the different output grating couplers. The goal of this experiment was to demonstrate a high degree of control over the light and validate the testbed's ability to measure high contrast ratios, making it an important precursor to the demonstration of actual coronagraphic functionality described in the next section.

With the input fiber aligned to the top input, loading the precalibrated bar state gave a starting ER of ~85 dB at a wavelength of 1550.0007 nm. The phase shifters on the mesh were then controlled to find the minimum possible signal in the bottom output channel (channel 0 in Fig. 4) by correcting the starting bar state and controlling the path of any light reflected from the output grating coupler back into the mesh.

Figure 6(a) shows the ER measured throughout the experiment, which reached a final ER of $3.83 \pm 0.8 \times 10^{-10}$ (over 94 dB). To our knowledge, this is the highest ER recorded for

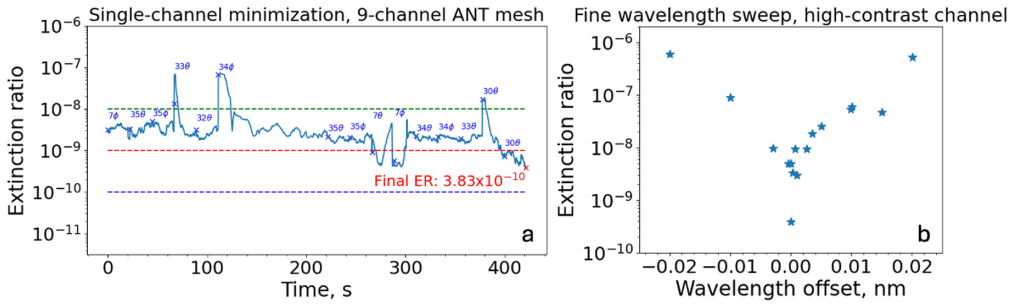


Fig. 6 (a) Data from a single-channel minimization experiment showing an extinction ratio of $3.83 \pm 0.8 \times 10^{-10}$ (>94 dB) using a 9×9 full triangular mesh at 1550.0007 nm wavelength. The blue crosses indicate the start of each minimization routine using the adjacent phase shifter number corresponding to the labels from Fig. 4. The green, red, and blue dotted lines mark 1×10^{-8}, 1×10^{-9}, and 1×10^{-10} exctinction ratios, respectively. (b) Extinction ratio as a function of wavelength offset from the 1550.0007 nm central wavelength.

suppressing a monochromatic signal on-chip, improving on the team's prior published result.[31] The uncertainty is calculated based on the variation of the output measurement during a post-minimization dwell for 60 s, which we believe to be driven by thermal drift from small corrections to the TEC temperature to maintain the set point. This thermal instability is also seen in Fig. 6(a) around 280 s, when the experiment reaches a high contrast but later degrades. The experiment continued until a setting was reached that could maintain the high-contrast state for longer than a few seconds. The signal in the top output channel (channel 8) was monitored throughout the experiment to detect changes due to misalignment of the input fiber caused by thermal expansion/contraction in the metal fiber holder. The input fiber position was periodically realigned to maximize the signal in the top output channel to maintain alignment throughout the experiment.

The wavelength dependence of the instrument was assessed by holding the voltages applied to the AstroPIC chip constant and sweeping the wavelength of the laser source. The resulting ERs are plotted as a function of wavelength offset from the central wavelength of 1550.0007 nm in Fig. 6(b), showing that the high ER is only achieved over a very narrow bandwidth of ~5 pm. In the future, testing will be conducted with a broadband laser source to experiment with broadband algorithms being developed by the team.[28] This monochromatic demonstration is a promising first step towards full coronagraphic performance and demonstrates the high stability and programmability offered by integrated photonics technology. These results also validate the AstroPIC testbed's ability to measure extremely high contrast ratios in the laboratory environment.

3.2 Mode Sorting of Multiple Input Channels

A key capability of the AstroPIC testbed is the ability to test the PIC coronagraph performance using realistic telescope pupil shapes. To enable this, a free-space coupling module has been designed and built at NASA Ames Research Center to compress a 3 mm diameter pupil shape by a factor of ten and reimage it onto the 300 μm wide 3×3 array of input grating couplers, shown in Fig. 7. The reimaged and compressed pupil is sampled by a 3×3 rectangular grid

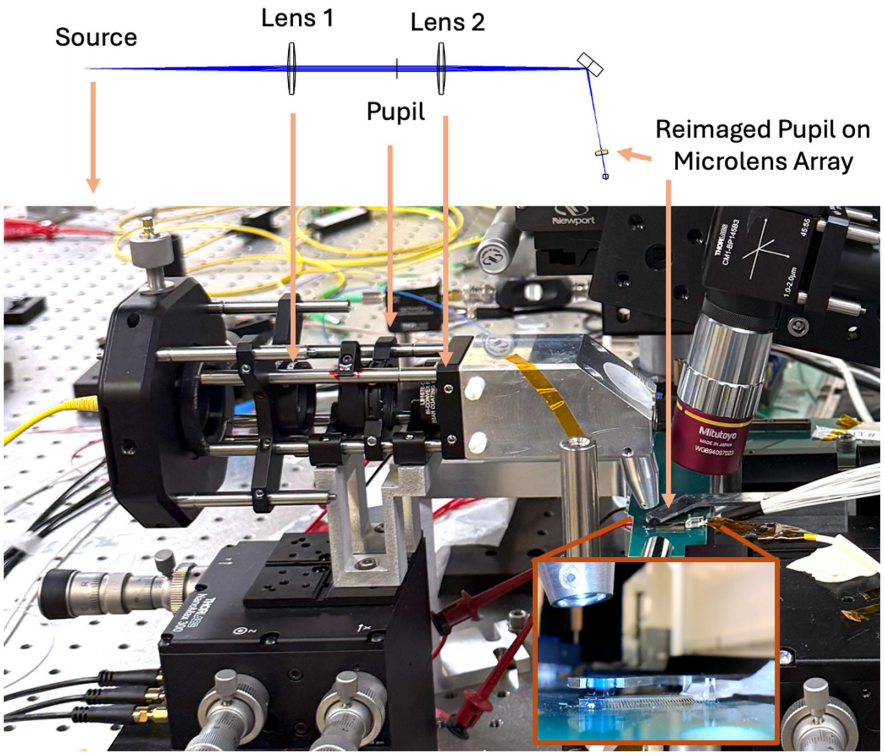


Fig. 7 (Top) ZEMAX™ ray trace model of free-space coupling module optical design with arrows indicating corresponding positions in (bottom) photo of free-space coupling module installed in the AstroPIC setup. A zoom-in image of the microlens array aligned above the PIC input is inset with a red border.

microlens array, which has a 100 μm pitch to match the grating coupler spacing. We selected the VIAVI MLA-S100-f4 off-the-shelf microlens array operating at $f/4.2$ which is close to the f/5 lens needed to match the size of the grating coupler mode. The input source is mounted in a cage-mountable XY stage with Polaris P20A piezoelectric actuators that can control the input source lateral position in order to change the output angle of the reimaged pupil.

For the first experiments with the free-space coupler module, a 4.3 mm circular pupil was inserted into the setup to emulate an unobstructed circular telescope aperture slightly overfilling the 300×300 μm input array of grating couplers. The throughput of the free-space coupler module with this pupil was measured to be 35%. A separate setup was constructed to characterize the free-space coupler by aligning the pupil output directly onto the focal plane array of a Goldeye G-030 SWIR camera as shown in Fig. 8(a). This setup was used to capture a photo of the reimaged circular pupil, shown in Fig. 8(b) with the 100 μm pitch input grating coupler array spacing overlaid for scale. This setup was also used to characterize the output angle of the reimaged pupil as a function of voltage applied to the piezoelectric actuators controlling the source launch position. To measure this, the camera focal plane was moved with a micrometer stage by a fixed amount to be further from the free-space coupler optics in order to defocus the pupil image and introduce a lateral displacement as a function of output angle. Then, the voltage applied to the X- and Y-axis piezoelectric actuators was swept from 0 to 150 V while recording images on the SWIR camera focal plane. The output pupil image center of mass (COM) in pixels was calculated for each applied voltage. An example of the defocused pupil image COM displacement as a

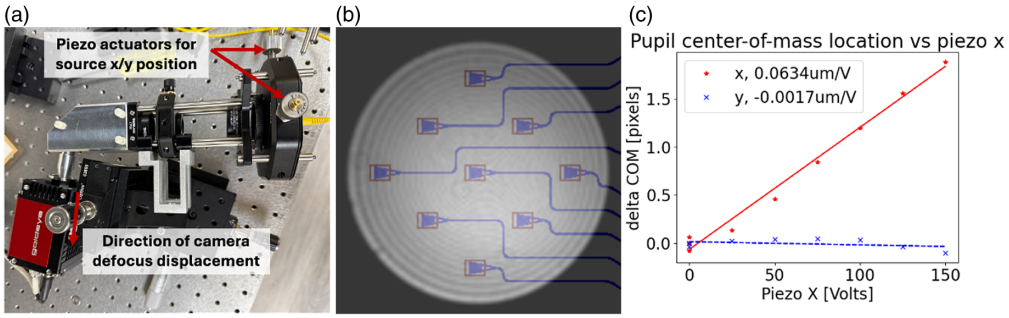


Fig. 8 (a) Optical setup used to image the free-space coupler output directly on a SWIR camera focal plane array. (b) Image of a 4.3 mm diameter circular pupil reimaged with the free-space coupler optics. (c) Defocused pupil plane image center of mass (COM) as a function of voltage applied to the piezoelectric actuator installed in the x-axis of the source mount. This linear fit was used to calculate the mapping between the applied voltage to the piezoelectric actuator and the output tilt angle of the reimaged pupil.

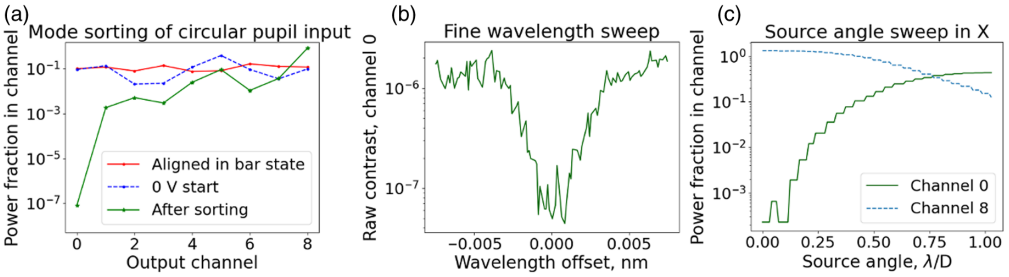


Fig. 9 (a) Power fraction in each output channel at different stages in the mode sorting experiment, showing a final raw contrast of $<1 \times 10^{-7}$ in channel 0. (b) Fine wavelength sweep showing the raw contrast in the high-contrast output channel (channel 0) as a function of wavelength offset from a central wavelength of 1550.007 nm. (c) Power fraction in output channels 0 (high-contrast channel) and eight (primary star channel) as a function of pupil source tilt angle sweep, showing an effective planet throughput into the high-contrast output channel 0 of >40%. Note: the photodetector gain needed to be reduced to avoid saturation in this measurement, so the minimum power at 0 source angle is below the noise floor of the photodetector.

function of applied voltage to the X-axis piezoelectric actuator is shown in Fig. 8(c) with a linear fit to the data. The slope of the COM displacement in μm versus applied piezo voltage fit was then mapped to effective angle per applied volt of 0.022 mrad/V using the known defocus displacement of the camera from the in-focus pupil location using the formula $\alpha = \arctan(\frac{\Delta x}{\Delta z})$ where α is the tilt angle, x is the lateral COM displacement, and z is the camera defocus displacement applied. This procedure was repeated for a range of camera defocus displacements to confirm that the resulting volt-to-angle mapping was repeatable and accurate. The total pupil tilt range provided by the piezoelectric XY actuators is measured to be $\sim 1\,\lambda/\mathrm{D}$ in both X- and Y-tilt.

The free-space coupler module was then installed into the testbed as shown in Fig. 7. The reimaged pupil was first aligned to couple into the input grating coupler array of the mesh, and then the microlens array was inserted to increase the coupling efficiency. The mesh was set to the precalibrated bar state to track the coupling into each input grating individually and ensure that the pupil was well aligned and providing balanced illumination to the input couplers. The amount of power measured in each input channel with the front end aligned and the mesh in bar state is plotted in solid red line in Fig. 9(a). The fraction of power in each of the nine channels is between 9% and 15%, which is close to ideal even illumination.

Once the free-space coupler was aligned to optimize coupling into the AstroPIC instrument, the 9×9 full triangular MZI mesh was used to implement the self-configuring mode sorting algorithm described in Miller 2013.[5] In this experiment, the mesh started with 0 V applied to all phase shifters, and the fraction of light in each output channel was recorded [blue dashed line labeled "0 V start" in Fig. 9(a)]. Then, each phase shifter along the upward diagonals of the triangular mesh was used in series to maximize the signal in the output channel corresponding to that diagonal. For instance, the first diagonal controlled the ϕ and θ phase shifters of MZIs 0 to 7 and maximized the signal in Output 8 using the labels in Fig. 4. This procedure has the effect of coherently adding the highest-power spatial mode and concentrating it into the top output.[5] Repeating this routine for the next diagonals further sorts additional spatial modes into corresponding output channels. After five diagonals had been controlled to pick out the five strongest spatial modes, there was no longer enough power remaining in the device to reliably run the coherent addition procedure, so the remaining actuators were tuned to directly minimize the signal in the bottom high-contrast output (channel 0).

This procedure eventually achieved a raw contrast of $8.7 \pm 1.1 \times 10^{-8}$ (Fig. 9), which is defined as the ratio of the signal measured in channel 0 divided by the total signal measured on the chip (accounting for the calibration factor to account for differences in output grating coupling efficiency between channels). This measurement uncertainty was calculated by taking the standard deviation of the signal recorded during a 30 s dwell after the minimized state was achieved. The wavelength dependence was measured by sweeping the laser source wavelength and recording the signal in the bottom output channel while maintaining the same minimized state phase shifter settings, shown in Fig. 9(b). The bottom output maintains high contrast over a narrow bandwidth of ~2 pm, but the team hopes to improve this in the future using a broadband laser source to test out algorithms that take advantage of the large number of degrees of freedom in the mesh to optimize the state to achieve deep contrasts across a broader bandwidth.[28]

To measure the effective throughput of the PIC coronagraph, the input source position was swept with the piezo actuator to tilt the incident field and record the signal in all the output channels. The photodetector gain needed to be reduced to avoid saturation during this measurement, which increased the noise floor of the measurement. Figure 9(c) shows the measured power fraction in channel 0 (high-contrast channel) and eight (primary star channel) as a function of incident source tilt angle. As the source angle increases, the relative power fraction in the primary star channel decreases while the relative power in the high-contrast channel increases to 43.5% at an angle of $1.03\,\lambda/\mathrm{D}$ (which is the maximum tilt angle that can be applied with the current free-space coupler design). This effective throughput measurement does not include losses due to on-off chip coupling and waveguide propagation loss, which were reported in Sec. 2.2, as these can be improved with new component designs[30] and waveguide material choice. In the future, the effective instrument throughput could be improved by applying different coronagraph operators to the mesh. For example, the mesh could be configured to a state that concentrates light from a certain angle into the high-contrast output channel if the planet's location is known in advance.

4 Discussion

Although these initial results are very promising, significant technology maturation is required for the AstroPIC concept to meet the requirements of a realistic coronagraph instrument. A companion paper in this special issue describes scientific yield analysis for the AstroPIC concept and its application to the HWO mission.[14] Here, we describe the next steps for four key areas for improvement: field of view, efficiency, contrast, and bandwidth.

The AstroPIC instrument field of view is directly related to the number of input channels (i.e., the number of grating coupler inputs along a side of the input array). A second-generation AstroPIC chip design is currently in progress that scales the instrument concept up from 9 to 16 input channels, increasing the outer working angle from 1.5 to $2\lambda/D$. For a full-scale coronagraph instrument, system-level mission yield studies indicate that the required number of channels will be ~400 to 1000, and that significant science returns are achievable even with fewer channels: an AstroPIC coronagraph with only 40 channels reaches ~ half of the total exo-Earth yield of a PIC coronagraph with 400 channels.[14,27] This is because exo-Earth candidates tend to have very small angular separations from their host star, which are accessible to PIC coronagraphs with modest channel counts. However, an AstroPIC instrument with >1000 channels is not infeasible as large-scale active PIC devices such as integrated optical phase arrays with thousands of channels and tens of thousands of active components have been demonstrated.[32,33]

The driving source of loss in the AstroPIC instrument is the coupling of light on and off of the chip through the grating couplers, which currently have a peak efficiency of ~35% and require the input light to be injected at a ~10 deg angle from normal, which introduces additional complexity into the instrument and testbed design. The second-generation AstroPIC prototype incorporates a higher-efficiency broadband grating coupler design[29,30] that has demonstrated a high coupling efficiency of 85% for a normally-incident cleaved optical fiber with a 1-dB bandwidth of 20 nm centered around 1546 nm wavelength, a significant improvement over the current design. This new normal-incidence grating coupler will greatly simplify the optical design for the front-end optics that re-image and couple a telescope pupil plane into the PIC and is expected to improve the end-to-end instrument efficiency from the current 3.6% to ~30%. To further improve the instrument efficiency, alternative photonic material platforms with lower propagation losses will be considered, as the current platform used by AstroPIC, silicon-on-insulator, has a typical loss of 1 to 2 dB/cm. In the NIR, silicon nitride[34] and doped-silica[35] platforms have both demonstrated propagation losses under 0.1 dB/cm. Another promising technology option is ultra-fast laser inscription in glass waveguides, which has demonstrated losses under 0.3 dB/cm and has been used to fabricate a 24-channel integrated MZI mesh with a total insertion loss of 4.35 dB.[36] These alternative platforms are also transparent over a larger wavelength range compared to silicon-on-insulator technology, which could be useful to extend the AstroPIC concept to a visible-light instrument.

Several improvements to the PIC and testbed design are planned to enable the AstroPIC coronagraph to reach the higher contrasts required for the HWO mission. The current experiments are hindered by stray light within the cladding of the chip reaching the output fibers and by back-reflected light from the output grating couplers that is able to reach the dark channel output. The new higher-efficiency grating coupler design should help with both of these sources of noise by reducing the amount of stray light and back-reflected light that does not couple into the output fiber. Increasing the isolation of the dark output channels from the rest of the chip could also be useful to prevent stray light from reaching the output channel. The device is also sensitive to small changes in the TEC temperature that can affect the coupling of stray light into the output fibers. This could be alleviated by operating experiments in a thermal vaccuum chamber, or the thermal control system for the chip could be reconsidered in the future to improve the stability of measurements at very low optical power levels. In parallel, nonthermal phase shifters should be considered for future iterations of the AstroPIC design, which would reduce the requirements on the thermal control system. Nonthermal phase actuators such as MEMS, piezoelectric, or electro-optic phase shifters[37] would provide additional benefits by eliminating thermal crosstalk between adjacent phase shifters and reducing the total power draw of the instrument.

The experiments presented in this work are all monochromatic using a near-infrared laser at 1550 nm wavelength, but a real PIC coronagraph will need to operate across a broader wavelength band to be useful for realistic astronomy applications. To address this, the AstroPIC team

is developing broadband PIC control algorithms targeting higher contrast across a broader optical bandwidth, which have been shown in simulation to achieve 10^{-10} contrast in a single channel over a 2.5% optical bandwidth.[28] The AstroPIC team plans to test these algorithms on the testbed using a broadband laser source in the future. The second-generation AstroPIC chip design will also include test structures for broadband 50:50 couplers that would reduce the chromaticity of the instrument. The current AstroPIC prototype is fabricated with silicon-on-insulator technology which is limited to the transparency range of the silicon waveguides (~1 to 3.5 μm), but other material platforms can extend the instrument concept to additional wavelength ranges, such as aluminum oxide (UV-visible[38]), silicon nitride (UV-mid IR[39]), silica-on-silicon (UV-mid IR[35]), femtosecond laser-written fluoride glass (UV - mid IR[40]), or thin-film lithium niobate (visible-mid IR[41]).

5 Conclusion

We have presented experimental results using the first-generation AstroPIC integrated photonic coronagraph prototype tested with the new integrated photonic testbed at NASA Ames Research Center. First, we have demonstrated a record-breaking extinction ratio of $3.83 \pm 0.8 \times 10^{-10}$, or over 94 dB, of a single input channel illuminated with monochromatic light at 1550 nm wavelength using a 9×9 full triangular MZI mesh. This was achieved by first setting a precalibrated bar state to the mesh and then tuning additional phase shifters to further minimize the signal and control the path of back-reflected light. This measurement validates the photonic testbed's ability to measure high contrast ratios and is an important intermediate step toward full coronagraphic performance. Achieving a contrast measurement on the order of 3×10^{-10} with bulk optics technology requires precise optical systems with advanced thermal control, typically operated in vacuum.[7,42] This demonstration of extremely high extinction ratio in a standard laboratory environment shows the power of integrated photonics technology to manipulate light with high precision using systems that are significantly smaller and less complex than traditional bulk optics designs.

We have also demonstrated free-space injection of a reimaged telescope pupil into the PIC coronagraph using a free-space coupler module. We used this module to couple light from a circular, unobstructed pupil into the 3×3 input grating coupler array using a microlens array aligned above the PIC input to improve coupling. The nine-channel full triangular MZI mesh was then used to implement a self-configuring mode sorting algorithm to coherently add the input light into different output channels based on their spatial mode. After sorting the source modes into four "bright" channels, the remaining MZI phase shifters were used to minimize the signal in a designated "dark" channel. This dark channel achieved a peak raw contrast ratio of $8.7 \pm 1.1 \times 10^{-8}$, or over 70 dB, relative to the total power coupled into the chip. The planet throughput of the system was measured to be >40% by changing the incident angle of the pupil using a piezoelectric actuator and recording the fractional power in each output channel. This is the first demonstration of high-contrast measurements using a PIC coronagraph operating with a realistic telescope-like pupil, representing an exciting step in advancing the technology readiness level of PIC coronagraphs.

The AstroPIC project is ongoing, and an upcoming second-generation prototype will scale up the instrument concept by increasing the number of input channels to 16 and incorporating higher-efficiency input grating couplers. Testing with the first-generation chip will continue with more detailed chip calibrations that will enable the team to test applying coronagraph operators directly to the mesh instead of relying on the self-calibrating mode sorting algorithm used in this work. The team is also in the process of procuring more pupil shape masks to replace the circular pupil in the free-space coupling optics to be more realistic to the HWO mission. This will allow the team to demonstrate the AstroPIC instrument's ability to achieve high contrasts in the presence of realistic mirror segment gaps and secondary struts, which is a major goal of the project.

Disclosures

The authors declare that there are no financial interests, commercial affiliations, or other potential conflicts of interest that could have influenced the objectivity of this research or the writing of this paper.

Code and Data Availability

Data presented in this paper can be made available upon reasonable request to the authors.

Acknowledgments

This work was carried out at NASA Ames Research Center and Stanford University's ECE department. The AstroPIC project is supported through NASA STMD's Early Career Initiative (ECI) program and the HWO Technology Maturation Project Office. The authors would like to express gratitude for administrative support from Kevin Sims, Naseem Rangwala, and Christine Martinez at NASA Ames Research Center.

References

1. S. Minardi, R. J. Harris, and L. Labadie, "Astrophotonics: astronomy and modern optics," *Astron. Astrophys. Rev.* **29**, 6 (2021).
2. L. Fineberg et al., "The Habitable Worlds Observatory engineering view: status, plans, and opportunities," *Proc. SPIE* **13092**, 130921N (2024).
3. W. Bogaerts et al., "Programmable photonic circuits," *Nature* **586**, 207–216 (2020).
4. M. Reck et al., "Experimental realization of any discrete unitary operator," *Phys. Rev. Lett.* **73**(1), 58–61 (1994).
5. D. A. B. Miller, "Self-configuring universal linear optical component [invited]," *Photonics Res.* **1**(1), 1–15 (2013).
6. O. Guyon et al., "Theoretical limits on extrasolar terrestrial planet detection with coronagraphs," *Astrophys. J. Suppl. Ser.* **167**(1), 81–99 (2006).
7. R. Belikov et al., "Theoretical Performance Limits for Coronagraphs on Obstructed and Unobstructed Apertures: How Much Can Current Designs be Improved?," *Proc. SPIE* **11823**, 118230W (2021).
8. J. B. Jewell et al., "A photonic coronagraph architecture achieving theoretical near ideal performance," *Proc. SPIE* **13092**, 130921S (2024).
9. D. McKeithen, J. Jewell, and J. K. Wallace, "Hardware development towards the demonstration of an ideal photonic coronagraph," *Proc. SPIE* **13092**, 130925V (2024).
10. E. Serabyn et al., "Nulling at short wavelengths: theoretical performance constraints and a demonstration of faint companion detection inside the diffraction limit with a rotating-baseline interferometer," *Mon. Not. R. Astron. Soc.* **489**, 1291–1303 (2019).
11. D. Echeverri et al., "Vortex fiber nulling for exoplanet observations: first direct detection of m dwarf companions around hip 21543, hip 94666, and hip 50319," *Astrophys. J. Lett.* **965**, L15 (2024).
12. B. R. M. Norris et al., "First on-sky demonstration of an integrated-photonic nulling interferometer: the glint instrument," *Mon. Not. R. Astron. Soc.* **491**, 4180–4193 (2019).
13. S. Martin et al., "TPF-interferometer: a decade of development in exoplanet detection technology," *Proc. SPIE* **8151**, 81510D (2011).
14. D. Sirbu et al., "Astropic: Architecture overview, science yield modeling, and technology status for the habitable worlds observatory2," *J. Astron. Telesc. Instrum. Syst.* **12**(4), 041028 (2026).
15. A. Boldin et al., "Reconfigurable free-space mode generation and detection enabled by an active photonic integrated circuit coupled to a passive mode-selective interface," *Commun. Phys.* **9**, 133 (2026).
16. V. Sharma et al., "Universal photonic processor for spatial mode decomposition," *Nat. Commun.* **16**, 7982 (2025).
17. S. SeyedinNavadeh et al., "Determining the optimal communication channels of arbitrary optical systems using integrated photonic processors," *Nat. Photonics* **18**, 149–155 (2024).
18. N. Deshler et al., "Experimental demonstration of a quantum-optimal coronagraph using spatial mode sorters," *Optica* **12**, 518 (2025).
19. Y. Xin et al., "Efficient detection and characterization of exoplanets within the diffraction limit: nulling with a mode-selective photonic lantern," *Astrophys. J.* **938**, 140 (2022).
20. Y. Xin et al., "Laboratory demonstration of a photonic lantern nuller in monochromatic and broadband light," *J. Astron. Telesc. Instrum. Syst.* **10**(2), 025001 (2024).
21. Y. J. Kim et al., "Coherent imaging with photonic lanterns," *Astrophys. J.* **964**, 113 (2024).
22. J. Lin et al., "Experimental and on-sky demonstration of spectrally dispersed wavefront sensing using a photonic lantern," *Opt. Lett.* **50**, 2780–2783 (2025).
23. M.-A. Martinod et al., "Scalable photonic-based nulling interferometry with the dispersed multi-baseline glint instrument," *Nat. Commun.* **12**, 2465 (2021).
24. P. Gatkine et al., "Efficient ultra-broadband low-resolution astrophotonic spectrographs," *Opt. Express* **32**, 17689–17703 (2024).
25. R. Morgan et al., "Testbed design and high-contrast demonstration with the astropic integrated photonic coronagraph," *Proc. SPIE* **13627**, 136270P (2025).

26. D. Sirbu et al., "AstroPIC: Near-Infrared photonic integrated circuit coronagraph architecture for the Habitable Worlds Observatory," *Proc. SPIE* **13092**, 130921T (2024).
27. D. Sirbu et al., "AstroPIC II: overview of technology development for a near-infrared photonic integrated coronagraph for the Habitable Worlds Observatory," *Proc. SPIE* **13623**, 1362309 (2025).
28. K. Fogarty et al., "Modelling and Optimization Pipeline for the AstroPIC Coronagraph," *Proc. SPIE* **13627**, 1362782 (2025).
29. C. G. Valdez et al., "High-efficiency vertically emitting coupler facilitated by three wave interaction gratings," *Opt. Lett.* **49**, 2373–2376 (2025).
30. C. G. Valdez et al., "Three-wave interaction grating coupler with the sub-decibel insertion loss at normal incidence," *Optica* **13**, 180–187 (2026).
31. C. G. Valdez et al., "High-contrast nulling in photonic meshes through architectural redundancy," *Opt. Lett.* **50**(11), 3660–3663 (2025).
32. J. Guglielmon et al., "Optical phased array super-cell beyond the reticle limit," in *CLEO*, Optica Publishing Group, p. STh5C.5 (2023).
33. C. V. Poulton et al., "8192-Element Optical Phased Array with 100 deg Steering Range and Flip-Chip Cmos," *[Conference on Lasers and Electro-Optics], Conference on Lasers and Electro-Optics*, Optica Publishing Group, JTh4A.3, 2020
34. K. Liu et al., "Ultralow 0.034-db/m loss wafer–scale integrated photonics realizing 720 million q and 380 μw threshold brillouin lasing," *Opt. Lett.* **47**(7), 1855–1858 (2022).
35. H.-J. Chen et al., "Towards fibre-like loss for photonic integration from violet to near-infrared," *Nature* **649**(8096), 338–344 (2026).
36. A. Barzaghi et al., "A 24-mode laser-written universal photonic processor in a glass-based platform," *Proc. SPIE* **13391**, 1339112 (2025).
37. H. Sun et al., "Silicon photonic phase shifters and their applications: a review," *Micromachines* **13**(9), 1509 (2022).
38. E. Mafakheri et al., "CMOS-compatible al2o3 low loss waveguides for ultraviolet photonics integrated circuits," *Proc. SPIE* **PC13369**, PC133690W (2025).
39. C. Xiang, W. Jin, and J. E. Bowers, "Silicon nitride passive and active photonic integrated circuits: trends and prospects," *Photonics Res.* **10**, A82 (2022).
40. T. T. Fernandez et al., "Ultrafast laser-fabricated fluoride glass waveguides with exceptionally high positive refractive index change for mid-infrared integrated optics," *Opt. Express* **32**, 42938–42950 (2024).
41. B. Desiatov et al., "Ultra-low-loss integrated visible photonics using thin-film lithium niobate," *Optica* **6**, 380 (2019).
42. B. Mennesson et al., "Current laboratory performance of starlight suppression systems and potential pathways to desired habitable worlds observatory exoplanet science capabilities," *J. Astron. Telesc. Instrum. Syst.* **10**(3), 035004 (2024).

Rachel Morgan is an optical scientist at the SETI Institute/NASA Ames Research Center. She specializes in applying integrated photonics technology to astrophysics instrumentation. She received her BS, MS, and PhD degrees in aerospace engineering in 2018, 2020, and 2023, respectively. Her PhD thesis focused on germanium-on-silicon integrated photonics for the mid-wave infrared wavelength range.

David A. B. Miller is the W. M. Keck Professor of Electrical Engineering Emeritus at Stanford University. His interests include nanophotonics, programmable photonics, and optics fundamentals. He has published >300 papers, two textbooks, and >75 patents. He has received several awards and two honorary doctorates; is a Fellow of AAAS, APS, OSA, IEEE, the Electromagnetics Academy, and the Royal Societies of London and Edinburgh; and is a Member of the US National Academies of Sciences and Engineering.

Dan Sirbu is a research scientist in the Astrophysics Branch at NASA Ames Research Center and serves as the PI of the AstroPIC project. His research interests are in high-contrast imaging of exoplanets, including photonic coronagraphs, wavefront control and estimation techniques, performance modeling and design of starlight suppression systems, and experimental validation.

Biographies of the other authors are not available.